

# Electron and lattice dynamics following optical excitation of metals

J. Hohlfeld, S.-S. Wellershoff, J. Güdde, U. Conrad, V. Jähnke, E. Matthias

*Fachbereich Physik, Freie Universität Berlin, Arnimallee 14, D-14195 Berlin, Germany*

Received 13 May 1999

## Abstract

New results about relaxation dynamics of optically excited electrons in metals, mostly gold and nickel films, are presented. Emphasis is on electron temperature near the surface as well as on the range of energy transport by ballistic and diffusive electron motion in comparison to the optical penetration depth. The experiments focus on the interval between creation of an electron temperature and the time at which thermal equilibrium between electrons and lattice is reached. Results were obtained by time-resolved *linear* and *second-harmonic reflectivity* measurements carried out in pump-probe mode. It is shown that the *two-temperature model* is well suited to describe hot electron diffusion in metals and to extract electron–phonon coupling constants from experimental data, provided corrections for ballistic electron motion are incorporated. The electron–phonon coupling constant of gold was found to be independent of film thickness down to 10 nm. For noble metals, probe reflectivities near the interband transition were related to electron temperatures by a proper model for the dielectric function. For transition metals such relation between reflectivity and electron temperature is more difficult. A new pump-pump-probe technique was introduced which allows to study hot electron relaxation by probing the reflectivity in thermal equilibrium between electrons and lattice. Also these results can be well described by the two-temperature model. Finally, the interface sensitivity of the second harmonic was utilized to detect vibrational motion and thermal expansion of ultrathin nickel films on Cu(001). © 2000 Elsevier Science B.V. All rights reserved.

## 1. Introduction

The response of metals to optical radiation is a classical topic treated in textbooks [1]. Fresnel formulas with complex index of refraction describe reflection, absorption, and transmission in case of thin films. The irradiated sample is heated by the absorbed energy density, determined by spot size and energy deposition depth. For cw radiation the excitation rate is low and the time between two local excitations is much longer than the relaxation rate by electron–electron and electron–phonon collisions [2–4]. Consequently, electrons and lattice are in time-averaged thermal equilibrium and heat diffusion into

deeper parts of the material takes place on a scale set by the lattice thermal diffusivity. Regarding the absorbed energy density, there is a decisive difference between cw and ultrashort pulse laser radiation. For example, assuming total absorption, a 1 ps laser pulse of 1  $\mu\text{J}$  deposits an energy density which is  $10^6$  times larger than what of a 1 W cw laser stores per picosecond. The consequence regarding the local density of excited electrons is dramatic. To see this, let us estimate the number of excited electrons per atom. In a homogeneous lattice with  $5 \times 10^{28}$  atoms/ $\text{m}^3$ , total absorption of a 1  $\mu\text{J}/\text{ps}$  pulse with photon energy of 2 eV distributed over 100  $\mu\text{m}^2$  irradiated area and an absorption depth of 20 nm will

lead to about 30 photons per atom, while for a 1 W cw laser it amounts to only  $5 \times 10^{-6}$  photons per picosecond per atom. Although the absorption cross section varies with electronic structure and laser frequency, it is justified to assume that an absorbed pulse energy of  $1 \mu\text{J}/\text{ps}$  excites in a metal of the order of 1 conduction electron per atom. Hence, it is intuitively clear that a collective hot electron temperature very different from the lattice temperature evolves by electron-electron collisions [5,6]. In contrast, with cw laser irradiation each excited electron cools individually generating a local hot spot which does not interact with the hot spot of another excited electron, and no collective electron temperature can develop. Of course, the same is true for short pulses of very small energy.

For subpicosecond laser pulses we have to distinguish three time intervals sketched in Fig. 1. At first, immediately after excitation, when the electrons are in a highly nonequilibrium state (see Fig. 1(a)) [5,6], two competing processes take place. One is ballistic

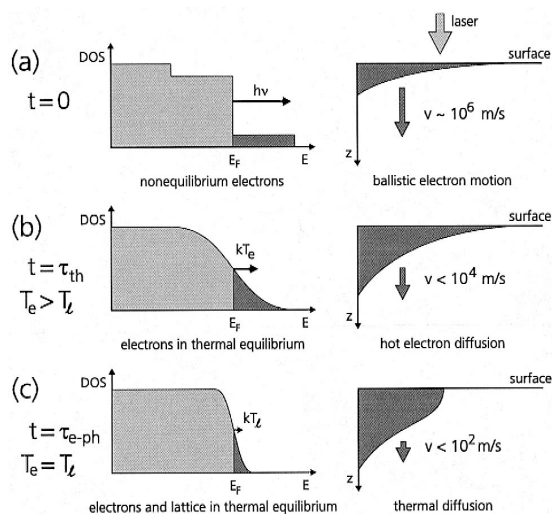


Fig. 1. Three distinguished relaxation phases of optically excited electrons in metals. (a) Photon absorption within the optical penetration depth generates at  $t = 0$  nonequilibrium electrons [5] which move with ballistic velocities into deeper parts of the sample [8]. (b) At  $t = \tau_{\text{th}}$  electrons have equilibrated by electron-electron collisions forming a Fermi distribution with a well defined electron temperature  $T_e$ , and diffusive energy transport starts within the electron gas. (c) Via electron-phonon coupling the electrons come into equilibrium with the lattice at  $t = \tau_{\text{e-ph}}$ , energy transport now proceeds by lattice thermal diffusion.

motion of these excited electrons into deeper parts of the sample with velocities close to the Fermi velocity, i.e., approximately  $10^6 \text{ m/s}$  [7–9]. For gold, a range of  $\approx 100 \text{ nm}$  was derived from fs time-resolved measurements [10,11], in good agreement with the calculated equilibrium value  $\Lambda = 117 \text{ nm}$  of the mean free path of electrons [12,13]. Similar values are obtained for all s/p-band metals, e.g.  $\Lambda(\text{Cu}) = 70 \text{ nm}$ ,  $\Lambda(\text{Ag}) = 142 \text{ nm}$ ,  $\Lambda(\text{Al}) = 46 \text{ nm}$ . For d-band metals we are not aware of any value for the ballistic range derived from femtosecond time-resolved measurements, but the estimated values of  $\Lambda$  are much smaller than for noble metals (e.g.  $\Lambda(\text{Ni}) = 11 \text{ nm}$ ,  $\Lambda(\text{Cr}) = 14 \text{ nm}$ ,  $\Lambda(\text{Mo}) = 20 \text{ nm}$ ) and of the same order as the optical penetration depth.

The other more general process is the development of an electron temperature by collisions between excited electrons and electrons around the Fermi level [14–17]. Once thermal equilibrium among hot electrons is reached, a second time interval starts which is characterized by the Fermi distribution (Fig. 1(b)) and an electron temperature which in the beginning differs strongly from the lattice temperature. Such hot electron bath is initially localized within either the ballistic range (for s/p-band metals) or the optical absorption depth (for d-band metals). Driven by the temperature gradient, these hot electrons diffuse into deeper parts of the bulk with a considerably slower speed than ballistic motion. The diffusion length is governed by electron-phonon coupling which cools the electron bath. In noble metals the weaker coupling leads to slower thermal relaxation and electron diffusion reaches much farther than in d-band metals [18] in which the electron temperature decays faster, thereby reducing the diffusion length [11]. Diffusive electron motion and cooling by electron-phonon coupling can be well described by the two-temperature model [19].

One can define a third time interval in which electrons and lattice have reached thermal equilibrium (Fig. 1(c)). Due to the vastly different heat capacities of electrons and lattice the equilibrium temperature rise is generally one to two orders of magnitude smaller than for electrons, and the remaining temperature gradient to still deeper parts of the metal is correspondingly weak. Hence, the final heat transport governed by this gradient and the lattice heat conductivity will be slow. Nevertheless, even in

this equilibrium regime the reflectivity is sufficiently sensitive to detect initial variations of electron temperature.

Ballistic motion and hot electron diffusion carry the absorbed energy into much greater depths of s/p-band metals than expected from the optical penetration depth. As a result, the final temperature of the near surface region is significantly lower than estimated from the inverse absorption coefficient. This will affect several applications. For example, in laser processing of metals much higher fluences than calculated from optical properties are needed to modify or ablate targets or films which are thicker than the electron diffusion range [20]. By the same token, thin metal films can be processed with significantly lower fluences [20,21]. Electron temperatures at the surface will also be important for femtosecond spectroscopy of adsorbates with strong coupling to the substrate [22–27].

The problem for the experimenter is how to measure electron temperatures,  $T_e$ , resulting from optical absorption. Non-contact techniques like optical reflection are ideal but require knowledge about the variation of reflectivity with  $T_e$ . In noble metals, the reflectivity of interband (d-s/p) transitions can be successfully utilized for this purpose. Fig. 2 shows the theoretically predicted [11,28] relative change in reflectivity  $\Delta R/R$  for Au at selected wavelengths. It is obvious that short wavelengths in the range 480–500 nm are best suited for detecting transient electron temperatures in Au. The relative change in reflectivity has a large magnitude and  $\Delta R/R$  scales

almost linearly with electron temperature. A linear relationship between  $\Delta R/R$  and  $T_e$  opens the way for a simple analysis of measured transient reflectivities.

Experiments were performed in pump-probe mode with the pump pulse heating the electron bath and the reflected probe pulse monitoring the electron temperature. The rule is that the wavelength of the pump pulse must be chosen in such a way that the reflectivity does not change significantly with electron temperature, i.e., that the self-action of the pump pulses must be negligible. For Au, this is the case at a wavelength around 400 nm as indicated by the solid line in Fig. 2. Consequently, this wavelength was chosen for the pump pulses in all investigations on Au presented here. Furthermore, the probe pulse should be weak to avoid much additional heating but its wavelength must guarantee a maximum change in reflectivity with electron temperature. In this contribution we discuss both *linear* and *second harmonic reflection* of probe pulses. Note that linear reflection registers a temperature averaged over the optical penetration depth. Nonlinear second harmonic generation (SHG) on centrosymmetric media, on the other hand, is much more surface sensitive and probes the electron temperature in the upper few surface layers. However, SHG is also capable of monitoring phonon excitations [29]. This fact becomes important in transition metals where electronic excitations are rapidly transferred to the lattice. In this context we will present new results obtained with time-resolved SHG demonstrating vibrational excitations and thermal expansion of thin Ni-films on Cu-substrates.

The correlation between reflectivity and electron temperature is of greater difficulty for transition metals with a more complex band structure near the Fermi level. To circumvent this problem a pump-pump-probe technique was invented in which the effect of a picosecond delay between two pump pulses on the reflectivity of a sample was probed in thermal equilibrium between electrons and lattice [30]. The advantages are twofold. One is that reflectivity changes of the probe pulse are proportional to temperature as long as the temperature variations are small. The other is that changes of reflectivity with temperature can be calibrated using temperatures which are easily accessible in the laboratory.

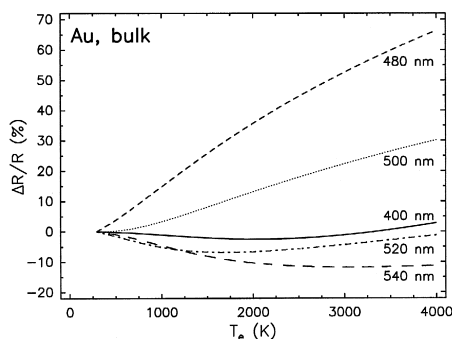


Fig. 2. Relative change of reflectivity with electron temperature at photon energies near the interband transition threshold in Au. The curves were calculated using a refined model [11,28,33] based on theories by Jah and Warke [31] and Rustagi [32].

## 2. Transient linear reflectivities

### 2.1. Interband transitions

For quasi-free electrons, light below the plasma frequency is partly absorbed and partly reflected from a metal surface but the dependence of reflectivity on electron temperature is usually weak. This changes completely when interband transitions (IT) are involved like, for example, d-s/p excitations in noble metals, as sketched in Fig. 3. Since the reflectivity varies with electronic occupancy it is evident that broadening of the Fermi distribution at elevated temperatures leads to increased absorption and decreased reflection for  $\hbar\omega < \text{ITT}$  (interband transition threshold), and the other way around for  $\hbar\omega > \text{ITT}$ . To illustrate this, calculated changes of the relative reflectivity  $\Delta R/R$  of gold ( $\text{ITT} = 2.47 \text{ eV}$ ) are plotted in the inset of Fig. 3 for various electron temperatures  $T_e$ . These curves are based on frequency and temperature dependence of the dielectric function  $\varepsilon(\omega, T_e)$  which we derived from models developed by Jah and Warke [31] and Rustagi [32] with some refinements described in Refs. [11,28,33].

In our experiments we excite conduction electrons with a pump pulse and monitor their relaxation by the reflectivity change of a probe pulse with varying delay. For the actual data analysis we use the nor-

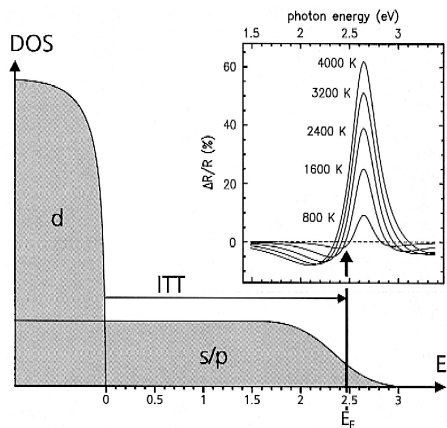


Fig. 3. Illustration of the density of states in gold at elevated electron temperatures. Calculated changes of relative reflectivities at energies near the interband transition threshold (ITT) are plotted in the inset for various electron temperatures.

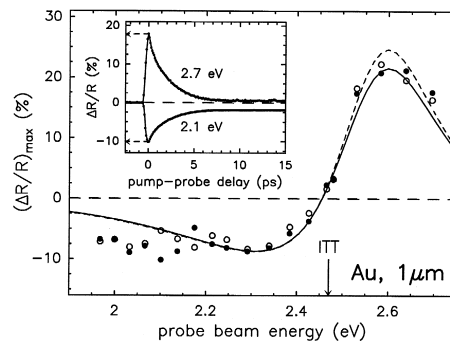


Fig. 4. Maximum changes of probe beam reflectivity obtained in pump-probe experiments on a  $1 \mu\text{m}$  thick polycrystalline gold sample with probe photon energies around the interband transition threshold (ITT). The measurements were performed with two probe beam polarizations:  $p-p$  (open symbols) and  $45^\circ-s$  (full symbols). The inset shows two typical pump-probe traces for  $45^\circ-s$  polarization from which data were taken. Dashed ( $p-p$ ) and solid ( $45^\circ-s$ ) lines show the result of model calculations for an electron temperature of 2700 K. For better comparison, the  $p-p$  data are divided by 1.8.

malized change in probe beam reflectivity, defined as

$$\frac{\Delta R}{R} = \frac{R(T_e) - R(293\text{K})}{R(293\text{K})}. \quad (2.1)$$

A first test of the model for the dielectric function consisted of verifying for a well defined pump fluence, i.e., a fixed electron temperature, the trend of  $(\Delta R/R)$  with photon energy around the interband transition threshold (ITT), shown in the inset of Fig. 3. To this purpose corresponding pump-probe measurements were carried out on a  $1 \mu\text{m}$  thick gold sample. Maximum values of the probe beam reflectivity change,  $(\Delta R/R)_{\text{max}}$ , taken from time-dependent measurements as shown in the inset, are plotted in Fig. 4 as a function of the photon energy of the probe beam. Data for two polarizations of the probe beam show the same trend, although there is some scatter towards lower energies. The observed variation with photon energy and the sign change at the ITT are in qualitative agreement with earlier results reported in Refs. [2,17]. Here, we demonstrate that the data in Fig. 4 can be described quantitatively by the model for  $\epsilon(\omega, T_e = 2700 \text{ K})$ , as shown by the dashed line for  $p-p$  polarization and the solid line for  $45^\circ-s$  polarization. The same quantitative agreement between model calculations and experi-

mental results are obtained for Cu bulk, as shown in Fig. 5. These variations of transient reflectivity with photon energies close to the ITT are a general feature for all noble metals.

## 2.2. Range of ballistic electrons

Fig. 3 illustrates that the reflectivity of interband transitions is quite sensitive to electron temperatures. In Ref. [10] we utilized this fact to investigate ballistic motion of non-equilibrium electrons in gold films by observing transient linear reflectivities in pump-probe mode. The concept of the experiment was that the initial spatial distribution of excited electrons moves with ballistic velocities into the film (cf. Fig. 1a). Electron–electron collisions broaden the distribution, slow down the motion and define a ballistic range. If, however, the film thickness is smaller than this range, the motion will be blocked and reflection at the substrate interface results in a higher energy density within the film. On the other hand, for film thicknesses exceeding this ballistic range electrons penetrate unhindered into greater depths which leads to smaller energy densities. Since the energy density is correlated to the electron temperature, we expect higher or lower electron temperatures, depending on whether the film thickness is smaller or larger than the ballistic range. This can be monitored by corresponding changes in probe beam reflectivity.

Thirteen Au-films of different thicknesses on fused silica were investigated in Ref. [10], varying from 10 to 100 nm in steps of 10 nm, and 200, 300, and 500 nm. Typical results for *s*-polarized probe pulses are depicted in the inset of Fig. 6. Two conspicuous

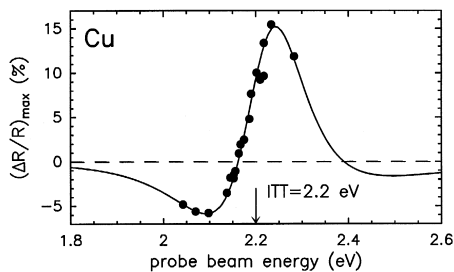


Fig. 5. Maximum reflectivity changes for polycrystalline copper (bulk). The measurements were performed with the *p*–*p* polarization combination. The solid line shows the result of model calculations with the ITT energy fitted to the data.

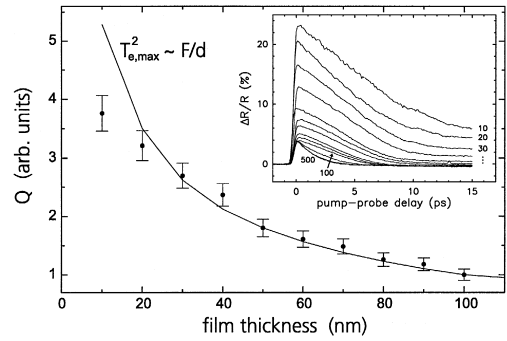


Fig. 6. Variation of maximum absorbed energy density  $Q$  with film thickness for gold films on fused silica derived from the data shown in the inset by identifying  $(\Delta R/R)_{\max}$  with  $T_{e,\max}$  and conversion into  $Q$  by Eq. (2.2). The solid line represents the proportionality  $Q \propto F/d$  normalized to unity at 100 nm thickness. The inset shows transient relative reflectivities recorded with 500 nm/100 fs *s*-polarized probe pulses. The numbers indicate the film thickness in nanometer. Pump pulses of 400 nm/200 fs were kept at an absorbed fluence of about 1 mJ/cm<sup>2</sup>.

effects can be noticed. One is the change of the decay character when increasing the thickness from 100 to 200 nm. A linear decay is found during the first 5 ps for film thicknesses up to 100 nm, while for 200 nm and thicker films the decay is closer to exponential. We interpret this alteration as being caused by a transition from homogeneously heated films (due to ballistic transport) to inhomogeneously heated films, where diffusive motion dominates the time-dependence of transient reflectivity. A more quantitative discussion of the data on the basis of the two-temperature model [19] in the next section will make this point clear.

The other more pronounced effect seen in the inset of Fig. 6 is the strong increase of  $\Delta R/R$  with decreasing thickness, signaling a corresponding increase in electron temperature. This unambiguously proves the pile up of energy density by reflection at the film-substrate interface. That the maxima of  $\Delta R/R$  indeed reflect the highest electron temperature can be verified by the following consideration. The energy density stored in an electron bath of temperature  $T_e$  is given by [33–35]

$$Q(T_e) = \frac{1}{2} A_e T_e^2, \quad (2.2)$$

since the heat capacity of the electrons is proportional to the electron temperature,  $C_e(T_e) = A_e T_e$ .

The absorbed energy density is given by the absorbed fluence  $F_{\text{abs}}$  divided by the deposition depth which, in turn, can be controlled by varying the film thickness  $d$ . We assume that the maximum change in reflectivity,  $(\Delta R/R)_{\text{max}}$ , corresponds to the highest electron temperature,  $T_{e,\text{max}}$ , which is reached before the absorbed energy couples to the lattice. Inserting explicit temperatures, this assumption holds when

$$T_{e,\text{max}}^2 = \frac{F_{\text{abs}}}{d} \frac{2}{A_e}. \quad (2.3)$$

Fig. 6 illustrates that this is indeed the case. The deviation of the value for 10 nm is most likely caused by film imperfections. The overall agreement between the data and the  $T_{e,\text{max}}^2$  dependence proves that ballistic energy transport causes a homogeneous energy distribution in Au-films up to 100 nm.

### 2.3. Two-temperature model

Thermal equilibrium among the excited electrons is reached within several hundred femtoseconds, depending on the excitation energy above Fermi level. Once it is established, we encounter the physical situation of a hot electron bath in a cold lattice which can be described by two separate temperatures,  $T_e$  and  $T_l$ . Cooling of the electrons proceeds by electron–phonon coupling and by diffusive motion. The temperature relaxation in time and sample depth can be modeled by two coupled diffusion equations, one describing the heat conduction of electrons and the other that of the lattice. Both equations are connected by a term that is proportional to the electron–phonon coupling constant  $g$  and to the temperature difference between electrons and lattice. The assumption that the electron–phonon coupling can be lumped into one linear coupling term of the form  $g \cdot (T_e - T_l)$  is the essence of the two-temperature model (TTM), originally proposed by Anisimov et al. [19]. It can be written in the form

$$C_e(T_e) \frac{\partial T_e}{\partial t} = \frac{\partial}{\partial z} \left( K_e \frac{\partial T_e}{\partial z} \right) - g(T_e - T_l) + P(\mathbf{r}, t), \quad (2.4)$$

$$C_l \frac{\partial T_l}{\partial t} = g(T_e - T_l). \quad (2.5)$$

Here,  $C_e$  and  $C_l$  are the respective heat capacities of electrons and lattice, and  $K_e$  is the thermal conductivity of the electrons. Since we are only interested in the relaxation dynamics that leads to thermal equilibrium of electrons and lattice, the heat conduction of the lattice was neglected. The source term

$$P(\mathbf{r}, t) = \frac{\alpha A I(\mathbf{r}, t) e^{-\alpha z}}{(1 - e^{-\alpha d})} \quad (2.6)$$

describes the absorbed energy density, determined by optical penetration depth  $\alpha^{-1}$ , film thickness  $d$ , and the absorbed fraction of the incident intensity  $A I(\mathbf{r}, t)$ , with  $A = (1 - R - T)$ . Here,  $R$  and  $T$  denote reflectivity and transmissivity, respectively. For thin films multiple reflection theory has to be employed to calculate the absorbed fluence [1].

The TTM can be solved numerically to predict the time dependence of  $T_e$  and  $T_l$ . A typical time evolution of electron and lattice temperatures at a gold surface is displayed in Fig. 7 for a bulk sample and a film of 20 nm thickness. The curves have been calculated with material constants listed in the figure caption. The main feature is the strikingly different thermal relaxation of bulk and film samples, caused

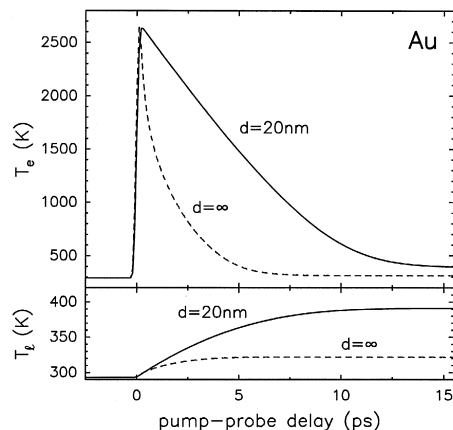


Fig. 7. Electron temperature relaxation at surfaces of bulk and 20 nm thick gold samples (upper curves) and lattice heating (lower curves) as predicted by the TTM. The following material constants were used:  $R = 0.408$ ,  $\alpha^{-1} = 15.328 \times 10^{-9}$  m,  $g = 2 \times 10^{16}$  W/m<sup>3</sup>K,  $K_{e,0} = 318$  W/mK,  $A_e = 67.96$  J/m<sup>3</sup>K<sup>2</sup>, together with the relations  $C_e = A_e T_e$  and  $K_e = K_{e,0} \times T_e / T_l$ . To obtain identical maximum electron temperatures, the absorbed fluence was 1.9 mJ/cm<sup>2</sup> for the bulk sample and 0.49 mJ/cm<sup>2</sup> for the 20 nm film.

by different depth distributions of the absorbed energy. In the thin film hot electron diffusion is inhibited and the energy is stored in a much smaller volume. The electrons cool exclusively by coupling to the lattice, resulting in a linear decay of the electron temperature during the first 7 ps. In the bulk sample, on the other hand, hot electrons diffuse into greater depths with the electron–phonon coupling governing the diffusion length. This diffusion leads to the fast almost exponential relaxation of  $T_e$  within about 3 ps. The final prediction is that, for a given fluence leading to an initial electron temperature rise to 2300 K, the bulk surface will only be heated by 30 K while the temperature of the 20 nm film increases by 100 K. The predicted change in the decay pattern at a bulk or thin film surface agrees qualitatively with the observations displayed in the inset of Fig. 6.

In principle, the Boltzmann equation would provide a more sophisticated mathematical model for electron cooling by diffusion and electron–phonon coupling [6,17]. Monte Carlo simulations [36] and comparison with experimental data prove, however, that the TTM is indeed a very good approximation as soon as an electron temperature exists. In the following we will present selected results to demonstrate the power of TTM in quantitatively reproducing experimental data. Note, however that some provision has to be made to incorporate the influence of ballistic motion and to include multiple reflection theory for the description of thin films.

In Fig. 8, transient reflectivities of four gold films with different thicknesses measured with 500 nm/100 fs probe pulses are compared to model calculations. The fit procedure was to first transform  $\Delta R/R$  into electron temperatures, using the model for  $\varepsilon(T_e)$  discussed in Refs. [11,28,33]. The second step was to fit TTM calculations to these electron temperatures by varying  $g$ . Model predictions indicated by dashed lines describe the results for the 20 nm film very well but fail for thicker films. For short times up to 1 ps model predictions strongly overshoot the experimental data. Also, for 300 and 500 nm films the measured reflectivities relax much slower than the calculated decrease. These deviations together with the good agreement for the 20 nm film indicate that the TTM underestimates the total energy deposition depth. In reality, this depth is enhanced by the ballistic motion of the electrons. We

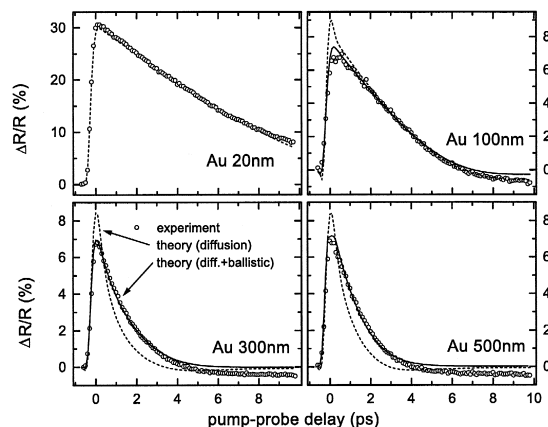


Fig. 8. Comparison of measured transient reflectivities with TTM predictions for gold films of different thickness. Notice that only the 20 nm film is within the ballistic range. Experimental data were taken with  $p$ -polarized probe pulses of 500 nm/100 fs and 400 nm/200 fs pump pulses of 1 mJ/cm<sup>2</sup> fluence. Dashed curves do not include a correction for ballistic energy transport, solid lines take a 105 nm ballistic range into account.

incorporated this effect into the TTM by adding the ballistic range to the optical penetration depth in the source term of Eq. (2.6), changing it to

$$P(z,t) = \frac{AI(t)e^{-z/(\lambda_s + \lambda_{\text{ball}})}}{(\lambda_s + \lambda_{\text{ball}})(1 - e^{-d/(\lambda_s + \lambda_{\text{ball}})})}. \quad (2.7)$$

Here,  $\lambda_s = \alpha^{-1}$ , and  $\lambda_{\text{ball}}$  is the ballistic range. In doing so, we neglect the initial time interval of about 100 fs needed for the ballistic electrons to penetrate 100 nm. As can be seen in Fig. 8, with this modification the TTM describes the experimental data well up to 5 ps when using  $\lambda_{\text{ball}} = 105$  nm. This value is in agreement with the qualitative conclusion drawn from Fig. 6. The small deviation for longer times is caused by a slight variation of reflectivity due to a change in band structure with lattice temperature [33], which is beyond the discussion here.

#### 2.4. Electron–phonon coupling constants

The two-temperature model can be used to determine the electron–phonon coupling constant of different metals. The simplest approach to do this is to utilize the linear decay of transient reflectivities for homogeneously heated thin films during the first few

picoseconds. The linearity in time can be understood in the following way. During the first few picoseconds the lattice remains cold and one can neglect Eq. (2.5). Furthermore, for film thicknesses smaller than the ballistic range the absorbed energy is homogeneously distributed throughout the film. Hence, there is no temperature gradient to drive hot electron diffusion and the term  $\frac{\partial}{\partial z}(K_e \frac{\partial}{\partial z} T_e)$  in Eq. (2.4) vanishes. Assuming that  $T_l \ll T_e$  and inserting the electronic heat capacity  $C_e = A_e T_e$  into the remaining equation, one obtains by integration a linear decay of  $T_e$  with time, starting at  $t = 0$  from the maximum temperature  $T_{e,\max}$

$$T_e(t) = T_{e,\max} - \frac{g \cdot (1 - T_{\text{room}}/T_{e,\max})}{A_e} \cdot t. \quad (2.8)$$

Thus, we learn that the observation of a linearly decreasing change in reflectivity is an unambiguous signature of the absence of hot electron diffusion. Taking the factor  $A_e$  from literature, the coupling constant  $g$  can be derived from the slope of the linear decay.

A representative example for such linear decay in a 30 nm gold film is shown in Fig. 9. The dashed line fitted according to Eq. (2.8) leads to a value of  $g = 2.1 \times 10^{16} \text{ W/m}^3\text{K}$  with an accuracy of about 10%. The agreement to a fit based on the numerical solution of the complete TTM displayed by the solid line is excellent. For films thinner than 100 nm the  $g$  values have been evaluated in a similar manner and are summarized in Fig. 11.

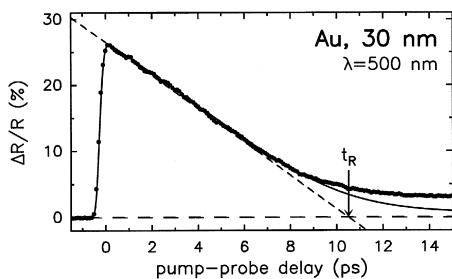


Fig. 9. Transient reflectivity for a 30 nm gold film. The dashed line is a fit to the data according to Eq. (2.8) up to 7 ps, whereas the solid line represents the solution of the complete TTM. The data were recorded with 400 nm/200 fs pump pulses of 1 mJ/cm<sup>2</sup> absorbed fluence and 500 nm/100 fs *p*-polarized probe pulses.

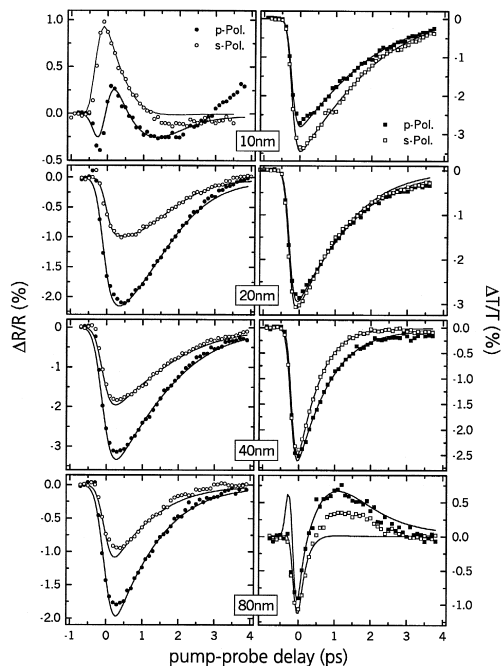


Fig. 10. Transient linear reflectivities (left panels) and transmissions (right panels) of gold films measured with *p*- (full symbols) and *s*- (open symbols) polarized probe pulses of 546 nm/100 fs. Pump pulses of 400 nm/200 fs were used and the absorbed fluence was about 0.7 mJ/cm<sup>2</sup>. Solid lines represent best fits to the data.

Any fit of the TTM to transient linear reflectivities depends on the relation between reflectivity and electron temperature and thus on the quality of the model used to calculate  $\epsilon(\omega, T_e)$ . An important quality test of this model is to examine changes in reflectivity and transmission at a different wavelength. To perform this test, we repeated the measurements on gold films with 546 nm/100 fs probe pulses, keeping the pump pulses at 400 nm/200 fs. The relaxation of  $\Delta R/R$  and  $\Delta T/T$  measured with *s*- and *p*-polarization is displayed in Fig. 10 for four different films. Solid lines represent best fits by the TTM with the coupling constant  $g$  being the only free parameter. Again, good agreement between theory and experiment is obtained, supporting both, the model for calculating  $\epsilon(\omega, T_e)$  and the TTM. Deviations observed for the transmission of *s*-polarized pulses through the 80 nm film lack significance due to the smallness of both absolute and relative change of transmission.



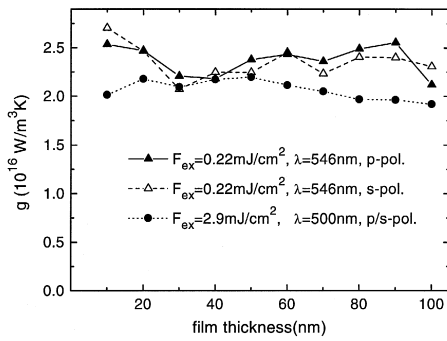


Fig. 11. Electron–phonon coupling constants for gold films between 10 and 100 nm, derived from fits of the TTM to transient reflectivities and transmissions. All values carry an uncertainty of 20%.

The data in Fig. 10 belong to gold films with thicknesses smaller than the ballistic range of 100 nm. Yet, we observe no linear decay as shown in Figs. 7–9. The reason for this is the nonlinear dependence of reflectivity and transmission on electron temperature (cf. Fig. 2) which becomes even more pronounced for thin films [11].

The successful modeling of the transient reflectivities opens the way to investigate whether the electron–phonon coupling constant depends on electron

temperature or film thickness. To investigate these two points, transient reflectivities of *p*-polarized 503 nm/100 fs probe pulses were measured on a 100 nm gold film for seven different pump fluences, where the highest one amounted to about one tenth of the damage threshold. No dependence of the coupling constant on electron temperature was observed.

Regarding the dependence of the coupling constant on film thickness, the compilation of all data is shown in Fig. 11. Although the individual values carry an uncertainty of about 20%, there is no discernible dependence on film thickness down to 10 nm. This observation is by no means trivial, considering that polycrystalline metal films on fused silica commonly grow in columnar structures and that the reduced dimensionality of thin films changes the phonon spectrum perpendicular to the surface [37].

Averaging over all data for two fluences and two wavelengths, we find from Fig. 11 an average coupling constant of  $g = (2.2 \pm 0.3) \times 10^{16} \text{ W/m}^3 \text{ K}$ , in good agreement with the values reported in the literature. All available information about electron–phonon coupling constants of gold is listed in Table 1.

The discussion of the results for gold is expected to apply likewise to other s/p-band metals. The next

Table 1

Summary of all electron–phonon coupling constants  $g$  of gold reported in the literature and derived from our transient reflectivity data. The value of  $g$  which is indicated by \* was determined from reported McMillan-factors  $\lambda\langle\omega\rangle^2$  via  $g = (3A_e\lambda\langle\omega\rangle^2)/(\hbar\pi k_B)$ . The following abbreviations are used: pc/sc, x = polycrystalline/single crystalline sample of thickness  $x$  in nm, R = transient reflectivity, T = transient transmission, PES = time-resolved photo-electron spectroscopy, SPP = time-resolved measurement of surface plasmon polariton resonance, surf. exp. = transient surface expansion measured by time-resolved probe beam deflection.  $\hbar\omega_{\text{pump}}$  and  $F_{\text{pump}}$  denote photon energies and pump fluences, respectively

Form	$g$ ( $10^{16} \text{ W m}^{-3} \text{ K}^{-1}$ )	Exp. techn.	$\hbar\omega_{\text{pump}}$ (eV)	$F_{\text{pump}}$ (mJ/cm <sup>2</sup> )	Ref.
pc, 30	* $2.65 \pm 0.5$	R(1.98 eV)	1.98		[18]
pc, 30	$3.0 \pm 0.5$	PES(5.52 eV)	1.84	0.4–1.6	[5]
pc, 20	$\approx 2$	R(eV)	1.24	$2.5 \times 10^{-3}$ –0.1	[17]
pc(sc), 20	4 ( $\leq 4$ )	R/T(2.02 eV)	2.02	0.7–4.0	[4]
pc(sc), 25–400	4 (3.5)	b-f R/T(2 eV)	2	0.1	[9]
sc, 30	$3.0 \pm 0.5$	SPP(1.97 eV)	1.97	0.3–1.3 J/cm <sup>3</sup>	[67]
pc, 470	$1.6 \pm 0.6$	surf. exp.	2.00	0.6	[68]
pc, 100	$\approx 2.7$	R(2.14 – 2.74 eV)	1.97	0.4, 4.0	[2,69]
pc, 20, 2500	$1.1 \pm 0.3$	R(2.00 eV)	2.00	1.2	[70]
pc, 10–500	$2.1 \pm 0.3$	R(2.48 eV)	3.10	2.9	this work
pc, 10–500	$2.3 \pm 0.3$	R/T(2.26 eV)	3.10	0.22	''
pc, 100	$2.0 \pm 0.2$	R(2.48 eV)	3.10	0.49–4.20	''
pc, 20–2000	$2.0 \pm 0.4$	damage threshold	3.10	8–120	''
pc, 2500	$2 \pm 1$	surf. exp.	1.55	5.6	''

question is whether the TTM equally well describes the electron relaxation in transition metals. Their more complex band structure near the Fermi level not only affects the reflectivity but also the electron–phonon coupling. To accentuate the typical difference between noble and d-band metals Fig. 12 shows a qualitative comparison of the transient reflectivities for various metals. All pump pulses were at 400 nm. Wavelengths of the probe pulses, indicated in the individual panels of Fig. 12, were chosen to provide an optimal sensitivity to temperature changes. Although no attempt is made to quantitatively describe the data, we want to point out some correlations between changes in reflectivity and electronic structure.

We recognize a characteristic s/p-electron pattern for gold and copper which only differs in relaxation times because copper has a 5 times larger electron–phonon coupling constant than gold. The essential point is that the weak electron–phonon coupling

allows the build-up of high electron temperatures and fast energy transport into deeper parts of the metal. This, in turn, results in a low equilibrium temperature at the surface. In contrast, the strong electron–phonon coupling of transition metals retains much of the absorbed energy near the surface but stored in the lattice. Depending on electronic structure, we observe a great similarity between chromium, molybdenum, and ruthenium. The platinum pattern lies somewhere between gold and molybdenum, indicating a hybrid action of d- and s-electrons. The s-electrons cause rapid diffusive energy transport while the d-electrons coupled to the lattice store part of the absorbed energy for longer times. In nickel the s-electron diffusion has receded and the d-electrons mediate energy storage in the lattice. Even more so, the cobalt pattern seems to be predominantly determined by the lattice temperature. It is unlikely that magnetization effects show up in these reflectivity changes. Although the transient reflectivities in Fig. 12 will change with probe wavelength, they obviously carry information about the electronic structure of the metals and it appears worthwhile to pursue this route in future. Here, we want to emphasize that the simple model used for noble metals is no longer applicable to describe the transient reflectivities of transition metals. The resulting uncertainty about the relation between electron temperature and reflectivity caused us to develop a technique which probes the reflectivity in thermal equilibrium between electrons and lattice for which temperature changes are sufficiently small to maintain a proportional response of the reflectivity.

## 2.5. Pump-pump-probe measurements

The applicability of the two-temperature model hinges on two requirements, the existence of an electron temperature and knowledge of  $R(T_e)$ . Regarding the latter, a theoretical model for the dielectric function was developed in Refs. [11,28,33]. For noble metals it correctly predicts the change in reflectivity with electron temperature in a wavelength range near the interband transition threshold. However, to apply this model to other wavelength regimes or, more generally, to d-band metals requires proper band structure calculations. To avoid complicated theories we pursued another approach, namely to

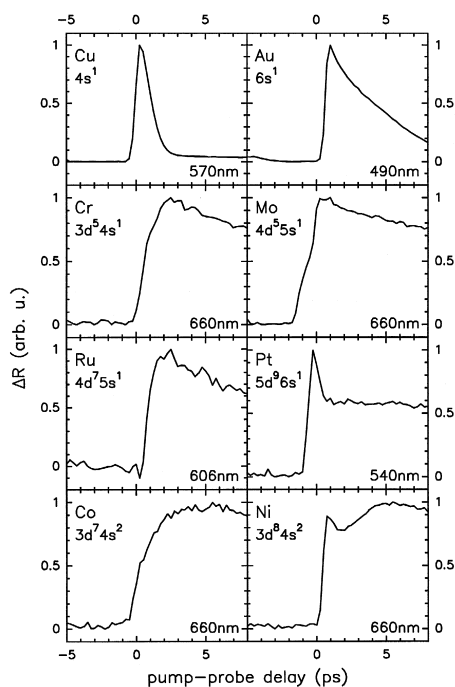


Fig. 12. Change of reflectivity for various metals to illustrate that deexcitation depends sensitively on electronic structure. Wavelength and fluence of the pump pulses were 400 nm and 1 mJ/cm<sup>2</sup>, respectively. Probe wavelengths used for the different metals are indicated.

probe the reflectivity in thermal equilibrium between electrons and lattice and to vary the effective pump intensity by utilizing two pump pulses [30] with mutual delay within the non-equilibrium time range to retain sensitivity to the electron–phonon coupling. The principle of this technique is sketched in Fig. 13.

As indicated, two pump pulses of identical fluence are delayed against each other in the picosecond range and the influence of such delay on reflectivity is measured much later when the electron temperature is completely relaxed. There are two advantages to this technique. One is that reflectivity changes are now recorded in a low temperature region where a proportionality  $\Delta R \propto \Delta T$  can be safely assumed. The other is that variations with temperature can be calibrated by heating the sample.

The linear relationship between temperature and reflectivity was tested experimentally for Au by monitoring for a 90 nm film the change of reflectivity with pump fluence at a probe pulse delay of 250 ps, where electrons and lattice are in equilibrium. The linearity extends from room temperature to the fluence threshold for melting and provides a calibration of  $\Delta R$  in terms of lattice temperature. Notice that the linear relationship  $\Delta R \propto T$  is no contradiction to Eq. (2.2) since in thermal equilibrium the heat capacity of the lattice is constant up to the melting point. Eq. (2.2), however, originates from the fact that the electronic heat capacity is proportional to  $T_e$ .

The physics of the pump-pump-probe technique is illustrated in Fig. 14 for a 90 nm gold film. Depicted are reflectivity variations probed by weak 490 nm/200 fs pulses for different delays of two pump pulses of 400 nm/200 fs and equal fluence. In these experiments both pump pulses were chopped and the total change of probe pulse reflectivity,  $\Delta R = R(T_e)$

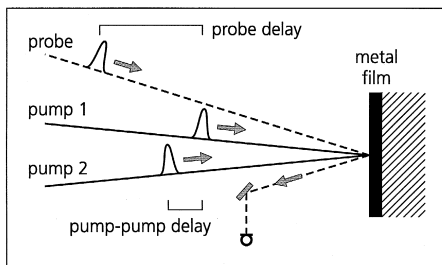


Fig. 13. Principal scheme of the pump-pump-probe technique.

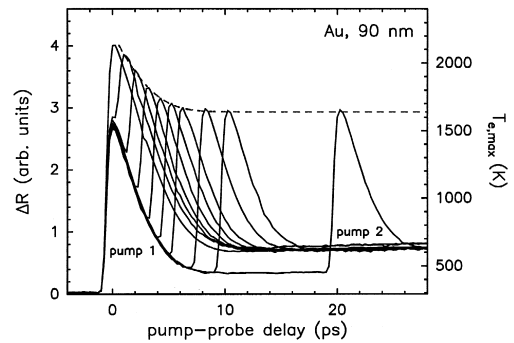


Fig. 14. Reflectivity changes of a 90 nm gold film at varying delays between two pump pulses of 400 nm/200 fs and a fluence of 1 mJ/cm<sup>2</sup> each. The reflectivity was probed by weak pulses of 490 nm/200 fs. The dashed line illustrates that  $T_{e,max}$  is proportional to the square root of the energy density within the electron gas.

–  $R(293K)$ , was recorded. According to Eq. (2.2)  $T_e$  and therefore  $\Delta R$  is proportional to the square root of the energy density deposited in the electron gas. Hence, when two pulses of equal fluence are superimposed, the reflectivity should change by a factor  $\sqrt{2}$  compared to delays of 10 ps or larger, where each pump pulse changes the reflectivity individually. This expectation is borne out by comparing the delayed pump pulse pattern to model calculations based on the TTM (dashed line) in Fig. 14. Important for applications, however, is the level remaining at longer times which keeps the reflectivity sensitive to changes in pump-pump delay.

Typical results obtained with the pump-pump-probe technique are shown in Fig. 15 for a 700 nm thick gold film. Displayed is the change in reflectivity  $\Delta R$ , measured with 490 nm/200 fs probe pulses as a function of delay between the two pump pulses. A conspicuous “dip” is observed when the pump pulses overlap, with wings that show the typical electron-lattice equilibration time. The size of the dip diminishes with increasing observation time, i.e., delay of the probe pulse. This dip originates from the nonlinear increase of electron diffusivity with temperature due to the term  $\frac{\partial}{\partial z}(K_e \frac{\partial}{\partial z} T_e)$  in Eq. (2.4). Two effects superimpose in the time range where  $T_e > T_l$ . An increased electron temperature speeds up diffusion by a steeper gradient, and the thermal conductivity of the electrons grows with electron temperature [38],  $K_e \approx K_0(T_e/T_l)$ . Hence, the higher

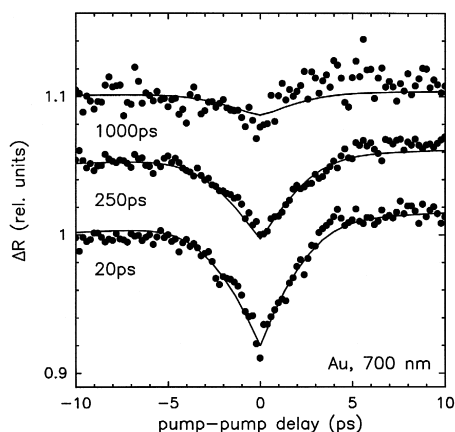


Fig. 15. Reflectivity changes of a 700 nm gold film as a function of delay between two pump pulses of 400 nm/200 fs and 1.5 mJ/cm<sup>2</sup> each. Three data sets were measured with 490 nm/200 fs probe pulses at the observation times indicated.  $\Delta R$  is plotted in relative units and the offset for longer probe delays is 0.05. The sloping base lines are caused by the fact that the observation time of the probe pulse refers to only one of the pump pulses.

the electron temperature, the faster the electron diffusion proceeds into the depth of the material. The consequence is a reduction of the resulting surface temperature generated by two superimposed pump pulses relative to what would be expected for the sum of two separated pulses which defines the reference line for large pump-pump delays. The important point is that the data in Fig. 15 can be perfectly reproduced by the TTM. The solid lines are not best fits but represent TTM calculations for gold with *no* free parameter.

The size of the dip will depend on observation time and film thickness. To substantiate this statement we performed TTM calculations in which either one of these two parameters was varied. Fig. 16 shows the results. Plotted are normalized changes in surface temperature which are equivalent to changes in reflectivity. The main result is that the dip vanishes as soon as the absorbed energy is homogeneously distributed throughout the sample, while it is largest when the lattice diffusive energy transport into the depth of the sample has just started. Thick films show larger dips because it takes longer to reach a homogeneous energy distribution than in thin films. This has been experimentally verified (see Fig. 2 of Ref. [30]). In the time domain, on the other

hand, the dip vanishes in the asymptotic limit where the heat is spread throughout the whole sample volume, and it is most pronounced for short observation times. The measured data in Fig. 15 confirm this. When probing at 1 ns the dip is barely discernible and amounts to less than 1%. However, when observed at 20 ps the “dip” reaches 7%.

Up to now we only discussed results for gold samples. The outset, however, was to develop a method which is applicable to all metals and to overcome the difficulty of deriving the time dependence of electron temperatures from transient reflectivities. The success of the new technique is illustrated in Fig. 17 which shows examples of pump-pump-probe results for copper, ruthenium and chromium samples. Again, two pump pulses of 400 nm/200 fs and 1.5 mJ/cm<sup>2</sup> each were applied, because at this wavelength the reflectivity is insensitive to electron temperature and optical properties at room temperature can be used in the source term. Probe wavelengths of 565, 660, 606 nm for copper, chromium, and ruthenium, respectively, guaranteed a good temperature sensitivity of the reflectivity. Observation times listed in the figure caption of Fig. 17,

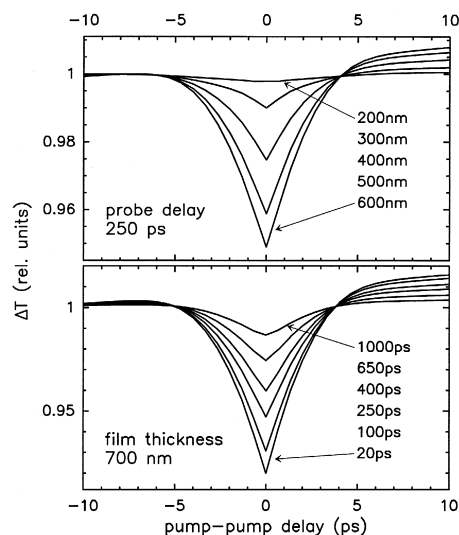


Fig. 16. Surface temperature changes for gold calculated as a function of mutual delay between the two pump pulses using the TTM. In the upper panel the observation time was kept at 250 ps and the film thickness was altered from 200 to 600 nm. The lower panel shows the surface temperature variation of a 700 nm film probed at observation times between 20 ps and 1 ns.

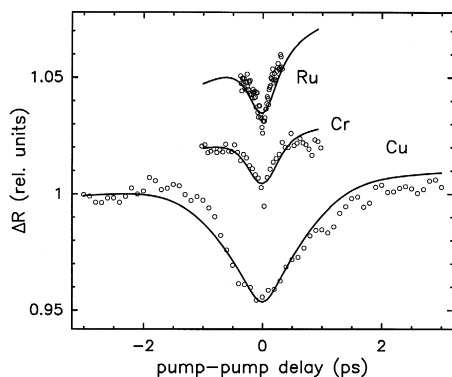


Fig. 17. Reflectivity changes for copper, chromium, and ruthenium as a function of pump-pump delay. Pump pulses of 400 nm/200 fs and 1.5 mJ/cm<sup>2</sup> fluence were applied in all cases. The reflectivity was probed by 200 fs pulses of 565 nm (Cu), 660 nm (Cr), and 606 nm (Ru) at delays of 15, 50, 15 ps, respectively. Solid lines are TTM calculations with no free parameters. The sloping background stems from the superposition of pump and probe delays.

were chosen to minimize the slope of the background without reducing the dip size. The solid lines represent TTM calculations with fixed parameters taken from literature and listed in Table 2. The good agreement between theory and experiment proves that it is possible to extract the electron–phonon coupling constant by analyzing pump-pump-probe data with the TTM. Summarizing all results obtained with this technique, two trends can be qualitatively

related to the material properties: 1. the width of the dip decreases with increasing electron–phonon coupling, 2. the amplitude of the dip scales roughly with the diffusivity of the sample.

### 3. Transient second harmonic generation

In this section we present new results on Au- and Ni-films obtained with time-resolved second harmonic generation (SHG) following excitation by a preceding pump pulse. The advantage of probing with nonlinear instead of linear reflectivity is the interface sensitivity of SHG which allows to selectively study the relaxation dynamics at surfaces and in thin films.

#### 3.1. SHG background

Second harmonic generation (SHG) originates from the nonlinear response of matter to intense light [39–41]. Considering only local contributions, the source of SHG is a nonlinear polarization which, in electric dipole approximation, has the form

$$P(\mathbf{r}, 2\omega) = \chi^{(2)}(\mathbf{r}) : \mathbf{E}(\mathbf{r}, \omega) \mathbf{E}(\mathbf{r}, \omega). \quad (3.1)$$

The nonlinear susceptibility  $\chi^{(2)}$  is a third rank tensor which vanishes in a surrounding of inversion symmetry. Therefore, in cubic metals it is generally

Table 2

Material constants used for TTM calculations. Listed are electron–phonon coupling constants  $g$ , electron specific heat constants  $A_e$ , and thermal conductivities  $K$  at  $T = 273$  K, taken from Ref. [65]. The thermal diffusivity  $\kappa$  was calculated using  $\kappa = K/C_l$  with values of  $C_l$  at  $T = 300$  K in Ref. [71]. If not otherwise indicated, the Debye temperatures  $\Theta_D$  were obtained from Ref. [72]. The optical penetration depths  $\alpha^{-1}$  and reflectivities  $R$  were calculated from optical constants at  $\lambda = 400$  nm reported in Ref. [73]

metal	$g$ ( $10^{16} \text{ W m}^{-3} \text{ K}^{-1}$ )	$A_e$ ( $\text{J m}^{-3} \text{ K}^{-2}$ )	$K$ ( $\text{W m}^{-1} \text{ K}^{-1}$ )	$\kappa$ ( $10^{-5} \text{ m}^2 \text{ s}^{-1}$ )	$\Theta_D$ (K)	$\alpha^{-1}$ (nm)	$R$ (%)
Au	2.1 <sup>a</sup>	71	318	12.8	165	16.3	39.1
Co	93 <sup>d</sup>	704	100	2.5	445 <sup>f</sup>	11.4 <sup>f</sup>	55.6 <sup>f</sup>
Cr	42 <sup>b</sup>	194	95	2.9	630	8.9	68.6
Cu	10 <sup>c</sup>	98	401	12.3	343	14.9	51.0
Mo	13 <sup>b</sup>	211	135	4.8	450 <sup>f</sup>	9.9	54.5
Ni	36 <sup>b</sup>	1065	91	2.2	450	13.5	48.0
Pt	25 <sup>d</sup>	740	73	2.6 <sup>e</sup>	240 <sup>f</sup>	11.2	55.5
Ru	110 <sup>d</sup>	400	117	4.1 <sup>e</sup>	600	6.9	71.0

<sup>a</sup> This work; <sup>b</sup> Ref. [20]; <sup>c</sup> Ref. [3]; <sup>d</sup> Ref. [33]; <sup>e</sup>  $T = 273$  K; <sup>f</sup> Ref. [65].

zero, except for a narrow surface layer which lacks inversion symmetry. In contrast, the linear optical response, described by a susceptibility tensor  $\chi^{(1)}$  of rank 2, is symmetric under inversion and stems from bulk polarization down to the optical penetration depth. Its surface sensitivity renders SHG an attractive technique for investigating properties of surfaces and interfaces in multilayer systems [41]. The price, however, is a minute yield which compared to linear reflectivities is reduced by many orders of magnitude, typically  $10^{12}$  for metals. Experimentally, this can partially be compensated by the excellent signal-to-noise ratio which can be achieved because it is easy to discriminate between light of frequencies  $\omega$  and  $2\omega$ .

To make use of the surface sensitivity of SHG is, however, not trivial because its yield is governed by both, the nonlinear susceptibility and the linear optics of fundamental and second harmonic radiation. According to a phenomenological model by Sipe et al. [42] the amplitude of the second harmonic field can, in dipole approximation, be written in the form

$$E(2\omega) = \frac{2i\omega}{c} F(2\omega) \chi^{(2)} f(\omega) |E(\omega)|^2 \delta z, \quad (3.2)$$

where  $\delta z$  denotes the effective depth of the second harmonic response  $\chi^{(2)}$ . In metals  $\delta z \approx 5/k_F$ , with  $k_F$  being the Fermi wavevector, since at this depth the density of conduction electrons has reached its constant bulk value [43]. The so-called Fresnel factors  $f(\omega)$  and  $F(2\omega)$  contain all optical information about the fundamental and second harmonic fields, like refractive indices, polarizations, and angles of incidence. Their explicit form can be found in Refs. [11,41,42,44]. For details and band structure calculations of  $\chi^{(2)}$  we refer to the papers by Luce and Bennemann [45] and Hübner [46].

The nonlinear susceptibility tensor for SHG at polycrystalline surfaces can be reduced by symmetry arguments to three independent elements [40]:  $\chi_{zxx} = \chi_{zyy}$ ,  $\chi_{xxz} = \chi_{yyz}$ , and  $\chi_{zzz}$ . Inserting these three elements into Eq. (3.2) one finds for the second harmonic fields the following expressions for the most important polarization combinations of funda-

mental (lower case letter) and second harmonic (capital letter):

$s - P$ :

$$E_P(2\omega) = \frac{2i\omega}{c} A_P \varepsilon(2\omega) F_s \chi_{zxx} t_s^2 |E_s(\omega)|^2 \delta z, \quad (3.3)$$

$45^\circ - S$ :

$$E_S(2\omega) = \frac{2i\omega}{c} A_S \chi_{xxz} f_s t_p t_s |E_{45}(\omega)|^2 \delta z, \quad (3.4)$$

$p - P$ :

$$E_P(2\omega) = \frac{2i\omega}{c} \left[ A_P F_c \chi_{xxz} 2f_c f_s t_p^2 + A_P \varepsilon(2\omega) F_s (\chi_{zxx} f_c^2 t_p^2 + \chi_{zzz} f_c^2 t_p^2) \right] |E_p(\omega)|^2 \delta z. \quad (3.5)$$

The Fresnel factors  $f$ ,  $F$ , and  $A$  are defined among the others in Ref. [28].

The size of the nonlinear susceptibility is determined by matrix elements, spectral resonances, and the Fermi distribution. In pump-probe experiments all three contributions will be affected by pump-induced elevated electron temperatures. Since  $\chi_{ijk}$  is a surface specific quantity, it is of interest to find out whether its relaxation behavior is equal to the transient electron temperature within the optical penetration depth. This requires the separation of linear and nonlinear optical contributions to SHG (see Eq. (3.2)). Expected wavelength and temperature characteristics of  $\chi^{(2)}$  are illustrated in Fig. 18a. We note that SHG on noble metals is resonantly enhanced when the photon energy of the fundamental approaches the ITT. The resonance enhancement is due to a combined action of Fresnel factors and second-order susceptibility  $\chi^{(2)}$  and is dominated by variations of the occupation number in the intermediate state [44,47–50]. This variation of  $\chi^{(2)}$  with electronic occupancy around the Fermi energy makes SHG sensitive to elevated electron temperatures (cf. Fig. 18b). Unoccupied states below the Fermi energy serve as intermediate states and amplify  $\chi_{ijk}$ , while occupied states above  $E_F$  reduce the nonlinear response. In this way  $\chi_{ijk}$  reacts to a broadening of the Fermi distribution opposite to the linear reflectivity, which can be seen by comparing Figs. 3 and 18. However, regarding SHG as a cascade process, the

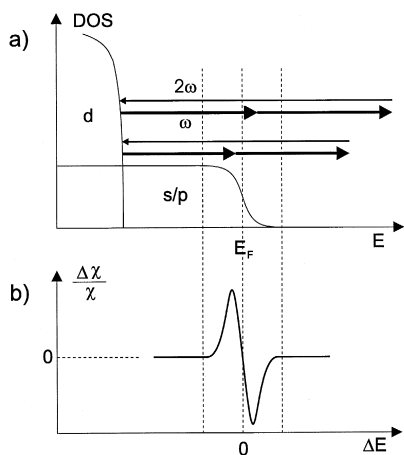


Fig. 18. Variation of  $\chi^{(2)}$  with energy mismatch  $\Delta E = \hbar\omega - \text{ITT}$  between the fundamental photon energy and the interband transition in noble metals. (a) illustrates the effect of electronic occupancy near the Fermi energy on the resonance enhancement in the lowest intermediate state, (b) shows the relative change of the nonlinear susceptibility.

response of  $\chi^{(2)}$  to electron temperatures is more complicated, since a reduced occupation number in the intermediate state will enhance the first excitation, but reduce the second one. An illustration of these interfering processes are provided by theoretical calculations of the electron temperature dependence of  $\chi^{(2)}$  for copper reported in Ref. [50].

### 3.2. Wavelength dependence of SHG on Au

All measurements on Au were conducted on a polycrystalline Au-film of 1  $\mu\text{m}$  thickness at room temperature in air. Pump pulses of 200 fs duration at a fixed wavelength of 400 nm excited the film at normal incidence. The absorbed pump fluence was about 7 mJ/cm<sup>2</sup>. The angle of incidence for the tunable probe-pulses of 70 fs duration was 45°. The ratios of fluences and spot diameters for the pump and probe pulses were about 20:1 and 6:1, respectively. SHG yields and linear reflectivities were detected using monochromators. Lock-in technique was used, improve the signal-to-noise ratio. When measuring static absolute values, the probe beam was chopped, whereas the time-resolved data were obtained with a chopped pump-beam.

We start by demonstrating the resonance enhancement of SHG due to interband transitions as a func-

tion of wavelength at a fixed temperature. Since such resonance enhancement is not only caused by  $\chi^{(2)}$  but by the Fresnel factors as well [44,47–50], we compare the wavelength dependencies of measured and calculated SHG yields normalized to unity at the ITT in Fig. 19. Experiments were done with three polarization combinations 45° – S, s – P, and p – P. The detected SHG yields were normalized to the square of the simultaneously recorded probe pulse intensities which are shown for comparison in the inset of Fig. 19. Theoretical calculations were done for the two polarization combinations 45° – S and s – P, since the p – P polarized SHG depends on the relative phases between three independent tensor elements (cf. Eq. (3.5)) which have not been determined experimentally. For the calculations a constant  $\chi^{(2)}$  is assumed and the variation with wavelength is only contained in the Fresnel factors. The similarity between calculated and measured SHG yields indicates that  $\chi^{(2)}$  does not strongly depend on wavelength around the ITT. When taking the square root of the experimental SHG yields divided by their Fresnel factors we find (not shown here) that the magnitude of the tensor elements depends indeed much weaker on wavelength than the total SHG yield. This observation is in line with results reported by Li et al. [47] who conducted SHG spectroscopy

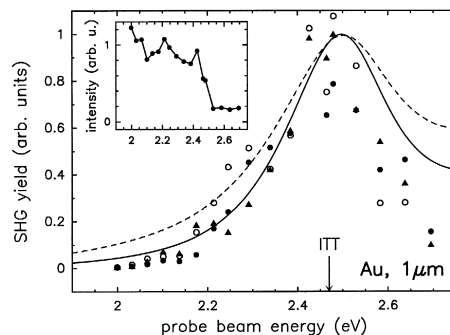


Fig. 19. SHG yield versus fundamental photon energy around the interband transition threshold. Plotted are the results obtained for three different polarization combinations p – P (full triangles), 45° – S (full circles), and s – P (open circles). The data for 45° – S and s – P are multiplied by 5 and 15 to match the p – P data. Solid and dashed lines represent calculated variations of SHG due to the wavelength dependence of Fresnel factors for the polarization combinations 45° – S and s – P, multiplied by 20.8 and 5.8, respectively, to reach unity at the ITT. The inset shows the energy dependence of the fundamental probe beam intensity.

on Ag(111) with the second-harmonic wavelength almost resonant to the ITT. These authors too found that the variations of SHG were dominated by Fresnel factors.

### 3.3. Temperature dependence for Au

Having examined the wavelength dependence of SHG on Au in the vicinity of the ITT at room temperature, we will now discuss variations of SHG yield with electron temperature utilizing fs-time-resolved pump-probe SHG. The goal is to extract the dependence of  $\chi^{(2)}$  on electron temperature in order to obtain information about the electron dynamics at the surface.

To start with, we want to present surprising new results on transient SHG yields measured for fundamental photon energies  $< 2.2$  eV. For these wavelengths complicated relaxation patterns are observed, as illustrated in Fig. 20 for  $p - P$  polarized SHG. These complex patterns arise from interference of linear and nonlinear reflectivities. Note that because of an identical pump fluence for all curves the

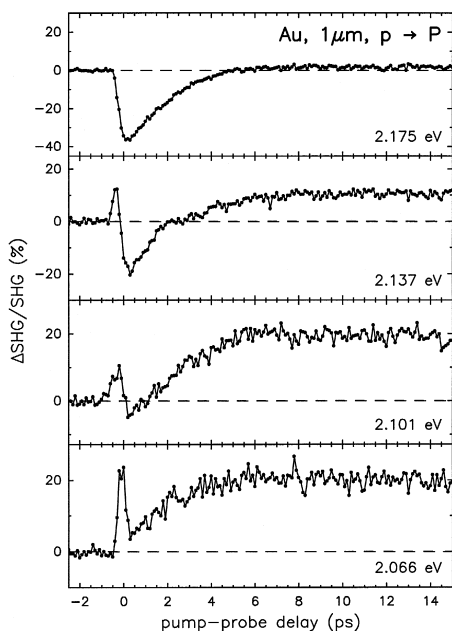


Fig. 20. Transient probe-SHG patterns at different probe beam energies for the polarization combination  $p - P$  on a thick Au sample. The same pump fluence was used to insure identical electron dynamics in all cases.

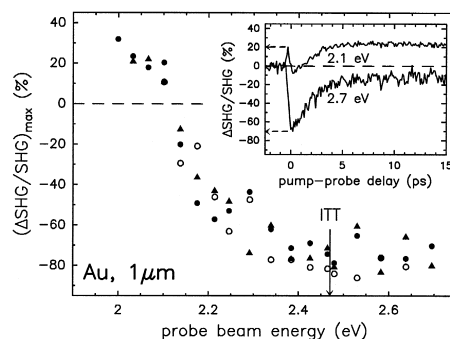


Fig. 21. Variation of transient SHG yield with photon energy around the interband transition threshold. Plotted is the SHG at maximum electron temperature for the three different polarization combinations  $p - P$  (full triangles),  $45^\circ - S$  (full circles), and  $s - P$  (open circles). The inset shows two typical pump-probe traces for  $45^\circ - S$  polarization and indicates the way data were taken. Notice that the sign change does not match the interband transition threshold.

maximum electron temperature is reached at the same time. When Fresnel factors and  $\chi^{(2)}$  respond differently to the electron temperature rise – in the sense that they change sign at different photon energies around the ITT – one can understand the alternating variation of SHG yield with pump-probe delay at various energies. To support this conjecture we plotted the first maximum of the transient SHG, as indicated in the inset of Fig. 21, as a function of fundamental photon energy for three polarization combinations. The result is displayed in Fig. 21 and shows a systematic trend of the data changing sign at 15% lower energies compared to the ITT. These data are the nonlinear counterpart of those displayed in Fig. 4. A comparison of the two shows three differences: 1. The sign of the data is opposite, as expected from Figs. 3 and 18b. 2. Zero crossing occurs at a different photon energy. While it matches the ITT in the linear case, it is significantly lower for the SHG. 3. The sensitivity of transient SHG to electron temperatures is considerably larger. The data in Fig. 21 also prove, that the magnitude of  $\Delta\text{SHG}/\text{SHG}$  does not depend on the polarization combination. This result is in line with the wavelength dependence of SHG in Fig. 19.

Variations of SHG and  $\chi^{(2)}$  with electron temperature are not identical in general, since the SHG may be strongly affected by a temperature depen-



dence of the Fresnel factors. Thus, we converted the values of  $\Delta\text{SHG}/\text{SHG}$  shown in Fig. 21 into corresponding relative changes of  $\chi^{(2)}$ . The calculational procedure was as follows: First, we fitted the time-dependencies of the simultaneously measured linear reflectivities for  $s$ - and  $p$ -polarized light by the model for  $\varepsilon(\omega, T_e)$  (cf. Section 2.1) and the TTM to obtain knowledge about the relaxation behavior of electron and lattice temperatures and the corresponding variations of the dielectric function with pump-probe delay. These time-dependent optical constants were then used to predict relative variations of SHG under the assumption of a constant  $\chi^{(2)}$ . Again, such prediction is only possible when the SHG is related to one single tensor element of  $\chi^{(2)}$ . Therefore this procedure was only performed for the  $45^\circ - S$  ( $\propto \chi_{yyz}$ ) and  $s - P$  ( $\propto \chi_{zyy}$ ) polarization combinations. As an example, the relative changes of  $|\chi_{yyz}|^2$  and Fresnel factors are shown in Fig. 22. Note that the Fresnel factors change sign change at about 4 ps which shows that they are in general more complex than the linear reflectivity. The sign change causes a faster decay of the measured SHG compared to the electron temperature relaxation which was obtained from linear reflectivity and which agrees completely with the decay of  $\chi_{yyz}$ . The analysis of other  $45^\circ - S$  data shows the same agreement in the whole energy range investigated.

From the above result one could conclude that the electron dynamics is similar at the surface and in the bulk. However, when measuring the transient SHG for different polarization combinations (as done in

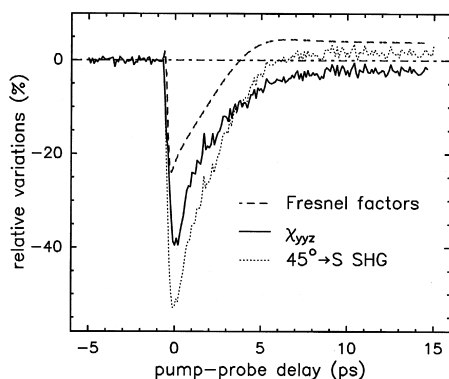


Fig. 22. Decomposition of transient  $45^\circ - S$  SHG (dotted line) into linear (dashed line) and nonlinear (solid line) parts. The measurement was done with 2.25 eV fundamental photon energy.

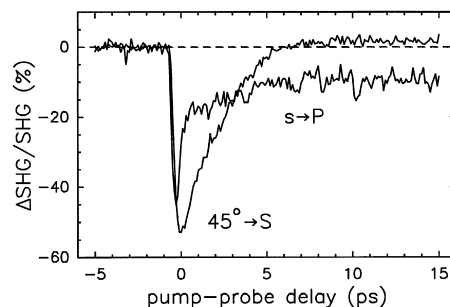


Fig. 23. Typical transient SHG traces for  $45^\circ - S$  and  $s - P$  polarizations recorded at a fundamental photon energy of 2.25 eV.

Fig. 21) we noticed strong differences in the relaxation patterns of  $45^\circ - S$  and  $p - P$  polarizations on the one hand, and  $s - P$  on the other. An example is shown in Fig. 23 for 2.25 eV fundamental photon energy, but similar deviations were observed at all energies larger than 2.2 eV. Since the calculated time-dependencies of the corresponding Fresnel factors show qualitative agreement, the observed deviations have to be related to the different tensor elements  $\chi_{yyz}$  and  $\chi_{zyy}$ . The transient SHG yields obtained with the  $45^\circ - S$  and  $p - P$  (not plotted) polarization combinations show a similar relaxation behavior as the simultaneously measured linear reflectivities. This observation is counterintuitive, since  $45^\circ - S$  contains only one tensor element while there are three in  $p - P$  (care for Eqs. (3.4) and (3.5)). Although the  $s - P$  polarization also contains only one tensor element (cf. Eq. (3.3)) it is distinctively different from the decay of  $45^\circ - S$ . The fast initial breakdown turns into a slow recovery at about 1 ps time-scale and relaxes very slowly from then on. This abrupt change in relaxation behavior indicates that transient SHG is not directly related to electron temperature when the electric field of the fundamental lies in the surface plane. This raises the question whether all tensor elements possess the same depth sensitivity. For  $s - P$  there exists no exciting electric field perpendicular to the surface, while for  $45^\circ - s$  an electric field excites anharmonic motion across the boundary. Therefore, it is conceivable that  $45^\circ - s$  indeed probes deeper into the material than  $s - P$ . This suggestion is supported by the fact that the longer decay of  $45^\circ - s$  is identical with the electron temperature relaxation recorded by transient linear reflectivity.

### 3.4. Ni-films on Cu(100)

In the preceding section we discussed how electron relaxation shows up in pump-probe-SHG measurements on gold surfaces and how the linear and nonlinear responses superimpose when working with a fundamental wavelength near the ITT. In this section we discuss transient SHG on ultrathin Ni-films deposited on a thermally conducting substrate. The interest here focuses on the interplay between electron relaxation and vibrational excitation as a function of film thickness. Nickel was chosen for several reasons. The growth of Ni-films on Cu(100) and its structural distortion is well understood [51–53]. Vibrational properties of this system have been studied both theoretically and experimentally [54–56]. The electron–phonon coupling strength of nickel is about 5 times larger than that of copper (cf. Table 2) leading to a rapid transfer of absorbed energy to the lattice. In addition, the thermal diffusivity of Ni is about 6 times smaller than that of Cu which ensures that the heat stays in the Ni-film much longer than near the substrate surface. Last not least, SHG at nickel interfaces is sensitive to small changes of electronic structure because of the large density of states at the Fermi level. Magnetic properties of the films will not be discussed here, for this topic we refer to the literature [57–59].

Nickel films were grown in UHV on Cu(100) surfaces, cleaned by repeated sputtering and annealing, and their thickness was controlled by medium energy electron diffraction (MEED) [60]. The SHG was generated by 150 fs/800 nm pulses of about 3 mJ/cm<sup>2</sup> fluence which struck the target at 45° angle of incidence with a repetition rate of 40 kHz. The second harmonic was recorded by lock-in detection. Great care was taken to avoid background SHG or depolarization caused by UHV windows.

Fig. 24 displays *p*–*P* polarized transient SHG of a 4 ML nickel film measured at a substrate temperature of 323 K where the film is still paramagnetic. Apart from the cross-correlation peak around zero delay (cut off in the display) the main feature is the exponential relaxation with a decay constant of 1.6(1) ps indicated by the dotted line [61]. It reflects cooling by hot electron diffusion into the cold substrate and compares well with the electron relaxation in copper [49]. The ratio of absorbed energy in the 4

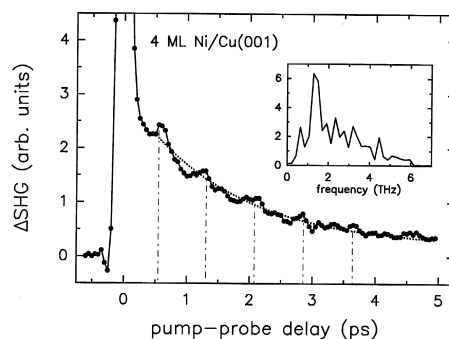


Fig. 24. Transient *p*–*P* polarized SHG recorded with 800 nm/150 fs pulses incident on a 4 ML nickel film on Cu(100). The fluence of the *p*-polarized pump pulses is about 12 mJ/cm<sup>2</sup>. The copper substrate was at 323 K. The exponential decay indicated by the dashed line has a time constant of  $(1.6 \pm 0.1)$  ps. Dashed-dotted lines mark the oscillation superimposed on the decay. Its Fourier transform is shown in the inset and results in a frequency of  $(1.4 \pm 0.2)$  THz.

ML nickel film and the copper substrate with an optical absorption depth of 12.5 nm is 1:2.6. This means the substrate is not substantially heated. Within the Ni-film the relaxation is predominantly by energy transfer to the lattice due to the larger electron–phonon coupling strength. In the copper substrate, on the other hand, the electron temperature relaxation is governed by hot electron diffusion and ballistic energy transport to the interior of the bulk (cf. Section 2.2). We must assume significant energy transfer from the nickel film into the substrate since otherwise the absorbed energy density in the film would lead to a lattice temperature rise of about 1100 K. Although the melting point of bulk nickel is about 1700 K we believe that the temperature limit for a stable film of a few monolayers is much lower. Efficient cooling by the copper substrate is confirmed by a decay constant compatible with that of copper [49]. Independent evidence comes from the magnetic splitting of the 7 ML film in Fig. 25, proving that the lattice temperature has dropped below the Curie point of 420 K at about 0.6 ps.

An interesting feature superimposed on the decay in Fig. 24 is the weak oscillation with maxima marked by the vertical dashed-dotted lines. Its Fourier analysis is displayed in the inset, yielding a frequency of 1.4(2) THz. We attribute this frequency to a coherent vibrational mode at the Ni-Cu interface, based on the following arguments: (1) At 4 ML

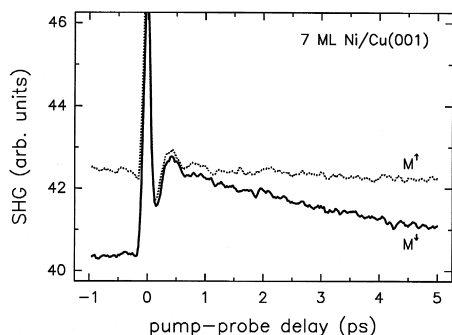


Fig. 25. Transient  $p$ – $P$  polarized SHG on 7 ML Ni/Cu(100) measured with 800 nm/150 fs incident pulses. The fluence of the  $p$ -polarized pump pulses is about  $12 \text{ mJ/cm}^2$ . Dotted and solid lines represent data for opposite directions of an external magnetizing field applied in the film plane but perpendicular to the plane of incidence. The splitting at negative delays corresponds to the magnetization of the film at a substrate temperature of 300 K.

thickness the SHG originates predominantly at the film-substrate interface but it is generated by the nickel band structure. The copper contribution to the SHG is negligible at the wavelength used [60]. (2) Due to absorption, the very different electron–phonon coupling strengths, and the unlike thermal properties of copper and nickel, the nickel film expands much more rapidly than the copper surface. This gives rise to an oscillation of the film against the substrate surface. (3) The vibrational frequency in Fig. 24 is about  $1/3$  of that of the Rayleigh mode measured at the  $\bar{X}$ -point [55]. Since SHG monitors the phonon modes around the  $\bar{\Gamma}$ -point we anticipate a lower frequency than those measured along the  $\bar{\Gamma}$ – $\bar{X}$  direction [55]. The observed value of 1.4 THz is still surprisingly large compared to calculated phonon dispersion curves of Ref. [56] for 4ML Ni/Cu(100). This points towards a sizeable wavevector which is probably caused by the reduced dimensionality and/or by film roughness. (4) We can exclude vibrational modes in the film, as reported in Ref. [55], because their frequencies are much higher.

The proposed vibration of the nickel film against the substrate is supported by a simple estimate of the frequency with which four Ni-ions oscillate against a fixed Cu-surface,  $\nu = (2\pi)^{-1} \sqrt{k_{\text{Ni-Cu}}/4m_{\text{Ni}}}$ . Lacking the force constant  $k_{\text{Ni-Cu}}$  we take the average of  $k_{\text{Ni-Ni}}$  and  $k_{\text{Cu-Cu}}$  reported in Ref. [62]. Inserting

$k_{\text{Ni-Cu}} = 33 \text{ kg/s}^2$  and  $4m_{\text{Ni}} = 2.29 \times 10^{-23} \text{ kg}$  we find a frequency of 1.46 THz in surprising agreement with the measured value. Similar oscillations were observed for 5 and 6 ML films with decreasing frequencies that fit a  $1/\sqrt{m}$  dependence. Apparently ultrathin Ni-films on a Cu-substrate are sufficiently elastic to respond to pulsed excitation with vibrational motion.

For films thicker than 6 ML the oscillation no longer develops due to strong damping which can be attributed to increasing roughness. This is illustrated in Fig. 25 for a 7 ML film. The transient SHG pattern for this thickness differs in several aspects from that of the 4 ML film. First of all, we observe a magnetic splitting [60] for opposite directions of an applied external field because the substrate temperature of 300 K lies below the Curie temperature of about 420 K for a 7 ML film [63]. The splitting at negative delays is a measure of the ferromagnetic coupling. During the first 700 fs the two curves for opposite magnetic field directions are identical within the noise level which proves that the Curie temperature of about 420 K was exceeded.

The second conspicuous feature in Fig. 25 is a deep minimum on the positive delay side of the cross-correlation peak followed by a maximum that starts a strongly damped oscillation. The electronic relaxation which was dominant in Fig. 24 now seems concealed by the background. We interpret this as follows. For 7 ML the SHG monitors less of the interface and more of the nickel surface, lowering contributions from copper electrons to the relaxation. Furthermore, the ratio of absorption between the 7 ML film and the substrate is now 1:1.5, and heat transfer to the substrate is reduced. Consequently, more energy is deposited in the film and lattice heating is more efficient which leads to a fast expansion of the film. The increased lattice spacing decreases the dispersion of the nickel d-bands which is equivalent to an increase of the density of states, in particular above the Fermi energy [64]. The result is an enhancement of the SHG. Hence, the steep rise between  $t = 0$  and the first peak near 0.4 ps is caused by the fast initial lattice expansion which then results in the damped oscillation depicted by the curves in Fig. 25.

Any lattice expansion propagates with the speed of sound characteristic of the film. Hence, if the

explanation given above for the first maximum around 0.5 ps in Fig. 25 is correct it must shift with film thickness. That this is indeed the case is illustrated in Fig. 26 for two films of greater thickness. We notice a peak shift from 0.8 ps for 16 ML to about 1.5 ps for 32 ML, and finally to 9.5 ps for 230 ML (not shown) which is not significantly changed by annealing the films (see dotted line for 32 ML). When plotting the film thickness versus appearance time of this first peak we find all points for thicknesses  $\geq 2.7$  nm ( $= 16$  ML) on a speed line of 4200 m/s, as shown in Fig. 27. The influence of slightly different substrate temperatures was ignored in the fit. This result is in excellent agreement with an estimate of the longitudinal speed of sound in a cubic crystal along the (001)-direction [65],  $v_\ell = \sqrt{c_{11}/\rho}$ . Inserting  $c_{11} = 16 \times 10^{10}$  N/m<sup>2</sup> from Ref. [65] and  $\rho = 8.9 \times 10^3$  kg/m<sup>3</sup> gives  $v_\ell = 4240$  m/s for Ni. We surmise that due to its surface sensitivity SHG is able to monitor the thermal expansion of thin films following pulsed optical excitation.

The inset of Fig. 27 shows a trend towards smaller sound velocities for very thin films. This tendency has been reported for metal films by Berberich et al. [66] and was attributed to stress in the films. Since in our case there is a 2.5% lattice mismatch between Ni

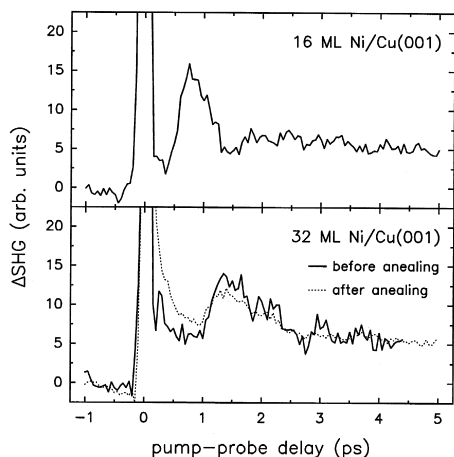


Fig. 26. Transient  $p$  –  $P$  polarized SHG curves recorded with 16 and 32 ML Ni/Cu(100) at 313 K substrate temperature. The pump-probe conditions were identical with those in Figs. 24 and 25. Solid lines were recorded with films as grown, the dotted line for 32 ML was measured with an annealed film 1 day after growth.

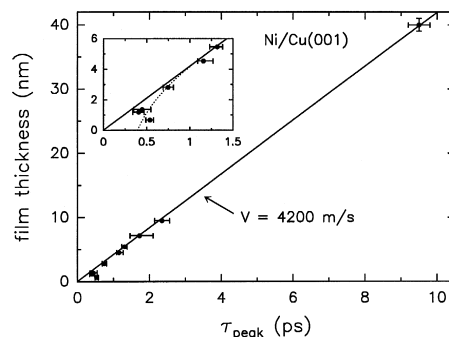


Fig. 27. Expansion speed of nickel films on Cu(100) derived from the occurrence time of the first maximum in the transient SHG curves like those shown in Figs. 24 through 26. All points above 2 nm are included in the fit (solid line). The inset shows the deviation of thin films from the speed line, converging to 0.35 ps (dotted line). A conversion factor 1 ML = 0.17 nm was used.

and Cu we expect that the observed effect is of same origin.

#### 4. Summary

The aim of this contribution was to study the spatial and temporal evolution of non-equilibrium energy distributions following optical excitation of metals. To do this we utilized pump-probe observation techniques in which a probe pulse tests, at variable delays, pump pulse induced changes in the electronic structure. Two modes were employed for probing, the linear reflectivity which averages over the optical penetration depth and second harmonic reflection which for centrosymmetric materials samples the surface layer. Most measurements were performed on gold and nickel films as representatives of noble and transition metals. With the exception of ballistic motion in gold, the investigations focussed on the dynamics of thermalized electrons.

For gold, sensitivity to electron temperature was achieved by choosing a probe wavelength near the interband transition threshold, and extensive studies of the wavelength dependence of linear and second harmonic reflectivities were carried out in this range. The goal of these studies was to emphasize the role of interband transitions for gaining information about electron temperature dynamics. The electron–phonon coupling constant of gold was found to be

independent of film thickness down to 10 nm and independent of pump fluence. Also, ballistic motion was detected in gold and its penetration depth was determined by varying the film thickness. There is no direct evidence for ballistic energy transport in *d*-band metals. If it exists, its range is within the optical penetration depths.

The great difference of electron–phonon coupling and energy transport between noble and transition metals was utilized for studying vibration and expansion of thin Ni-films on Cu-substrates with pump-probe SHG. For thin films below 7 ML the *interface* sensitivity of SHG allowed to observe the vibrational motion of the film against the substrate. In contrast, for thicker films we exploited the *surface* sensitivity to measure their thermal expansion and to derive the speed of sound in these films.

The validity of the two-temperature model and its usefulness to extract electron–phonon coupling strength was discussed in detail. We found that the model is well capable of describing the experimental data provided the absorbance entering the source term is known. Conversion of probe beam reflectivities into electron temperatures was achieved for noble metals by an appropriate model which has been counter-checked by wavelength and fluence dependencies of linear reflectivities. For transition metals such model would be more involved because the linear reflectivity is strongly governed by lattice temperature. For this reason a new method was introduced to measure the electron–phonon coupling in transition metals. It employs two pump pulses with mutual delay in the picosecond range and probes the linear reflectivity change at a much later time when electrons and lattice are in equilibrium. Measurements with this technique show a *characteristic drop in surface temperature* when both pump pulses are superimposed. Since the amplitude is a few Kelvin a linear relationship between reflectivity and temperature can be assumed. The two-temperature model describes this drop correctly for all metals tested, with no free parameter in the calculation.

In conclusion, we have shown that in gold ballistic and diffusive transport of hot electrons to the interior of the sample leads to considerable lower surface temperatures than anticipated from the energy density calculated using the optical penetration depth. We expect this result to be valid for all

s/p-band metals. In transition metals like nickel the strong electron–phonon coupling diminishes such energy transport to the depth. Instead, the electron excitation is rapidly transferred to the lattice causing vibrations of thin films and fast thermal expansion of thicker samples.

## Acknowledgements

This work was supported by the Deutsche Forschungsgemeinschaft, Sonderforschungsbereich 290. The authors thank Professor K.H. Bennemann for many helpful discussions and Mischa Bonn for the fruitful collaboration on pump-pump-probe experiments.

## References

- [1] M. Born, E. Wolf, Principles of Optics, 6th ed., Pergamon Press, Oxford, 1980.
- [2] R.W. Schoenlein, W.Z. Lin, J.G. Fujimoto, G.L. Eesley, Phys. Rev. Lett. 58 (1987) 1680.
- [3] H.E. Elsayed-Ali, T.B. Norris, M.A. Pessot, G.A. Mourou, Phys. Rev. Lett. 58 (1987) 1212.
- [4] H.E. Elsayed-Ali, T. Juhasz, G.O. Smith, W.E. Bron, Phys. Rev. B 43 (1991) 4488.
- [5] W.S. Fann, R. Storz, H.W.K. Tom, J. Bokor, Phys. Rev. Lett. 68 (1992) 2834.
- [6] W.S. Fann, R. Storz, H.W.K. Tom, J. Bokor, Phys. Rev. B 46 (1992) 13592.
- [7] S.D. Brorson, J.G. Fujimoto, E.P. Ippen, Phys. Rev. Lett. 59 (1987) 1962.
- [8] C. Suárez, W.E. Bron, T. Juhasz, Phys. Rev. Lett. 75 (1995) 4536.
- [9] T. Juhasz, H.E. Elsayed-Ali, G.O. Smith, C. Suárez, W.E. Bron, Phys. Rev. B 48 (1993) 15488.
- [10] J. Hohlfeld, J.G. Müller, S.-S. Wellershoff, E. Matthias, Appl. Phys. B 64 (1997) 387, notice the printing error in Eq. (1) which should be read:  $C_e(T_e)\partial T_e/\partial t = \partial/\partial z(K\partial T_e/\partial z) - g(T_e - T_l) + P(z, t)$ .
- [11] J. Hohlfeld, U. Conrad, J.G. Müller, S.-S. Wellershoff, E. Matthias, in: Nonlinear Optics in Metals, K.H. Bennemann (Ed.), Clarendon Press, Oxford, 1998, Chap. 3.
- [12] The mean free path of electrons was calculated by  $\Lambda = 3 \cdot K/(C_l \cdot c_L)$ , where  $K$  denotes the heat conductivity,  $C_l$  is the lattice heat capacity, and  $c_L$  is the speed of longitudinal phonons [13].
- [13] N.W. Ashcroft, N.D. Mermin, Solid State Physics, 1st ed., Saunders College Publishing, Philadelphia, 1976.
- [14] M. Aeschlimann, M. Bauer, S. Pawlik, W. Weber, R. Burgermeister, D. Oberli, H.C. Siegmann, Phys. Rev. Lett. 79 (1997) 5158.

- [15] M. Aeschlimann, M. Bauer, S. Pawlik, Chem. Phys. 205 (1996) 127.
- [16] C.-K. Sun, F. Vallée, L.H. Acioli, E.P. Ippen, J.G. Fujimoto, Phys. Rev. B 48 (1993) 12365.
- [17] C.-K. Sun, F. Vallée, L.H. Acioli, E.P. Ippen, J.G. Fujimoto, Phys. Rev. B 50 (1994) 15337.
- [18] S.D. Brorson, A. Kazeroonian, J.S. Moodera, D.W. Face, T.K. Cheng, E.P. Ippen, M.S. Dresselhaus, G. Dresselhaus, Phys. Rev. Lett. 64 (1990) 2172.
- [19] S.I. Anisimov, B.L. Kapeliovich, T.L. Perel'man, Sov. Phys. JETP 39 (1974) 375.
- [20] S.-S. Wellershoff, J. Güdde, J. Hohlfeld, J. Müller, E. Matthias, SPIE 3343 (1998) 378.
- [21] S. Preuss, E. Matthias, M. Stuke, Appl. Phys. A 59 (1994) 79.
- [22] F. Budde, T.F. Heinz, M.M.T. Loy, J.A. Misewich, F. de Rougemont, H. Zacharias, Phys. Rev. Lett. 23 (1991) 3024.
- [23] L.M. Struck, L.J. Richter, S.A. Buntin, R.R. Cavanagh, J.C. Stephenson, Phys. Rev. Lett. 77 (1996) 4576.
- [24] M. Brandbyge, P. Hedegård, T.F. Heinz, J.A. Misewich, D.M. Newns, Phys. Rev. B 52 (1995) 6042.
- [25] J.A. Misewich, A. Kalamarides, T.F. Heinz, U. Höfer, M.M.T. Loy, J. Chem. Phys. 100 (1994) 736.
- [26] F. Budde, T.F. Heinz, A. Kalamarides, M.M.T. Loy, J.A. Misewich, Surf. Sci. 283 (1993) 143.
- [27] J.A. Misewich, T.F. Heinz, D.M. Newns, Phys. Rev. Lett. 68 (1992) 3737.
- [28] J. Hohlfeld, D. Grosenick, U. Conrad, E. Matthias, Appl. Phys. A 60 (1995) 137.
- [29] Y.M. Chang, L. Xu, H.W.K. Tom, Phys. Rev. Lett. 78 (1997) 4649.
- [30] M. Bonn, D.N. Denzler, S. Funk, M. Wolf, S.-S. Wellershoff, J. Hohlfeld, Phys. Rev. B, in press.
- [31] S.S. Jha, C.S. Warke, Phys. Rev. 153 (1967) 751.
- [32] K.C. Rustagi, Il Nuovo Cimento B LIII, 1178 (1968).
- [33] J. Hohlfeld, Ph.D. thesis, Freie Universität Berlin, 1998, Verlag für Wissenschaft und Forschung, Berlin.
- [34] D. Pines, P. Nozières, The Theory of Quantum Liquids, W.A. Benjamin, New York, 1966, vol. 1.
- [35] W. Greiner, L. Neise, H. Stöcker, Thermodynamik und Statistische Mechanik, vol. 9 of Theoretische Physik, 1st ed., Verlag Harri Deutsch, Frankfurt am Main, 1987.
- [36] P. v. Hall, 1998, private communication.
- [37] A. Melikyan, H. Minassian, A. Guerra III, W. Wu, Appl. Phys. B 68 (1999) 411.
- [38] P.B. Corkum, F. Brunel, N.K. Sherman, T. Srinivasan-Rao, Phys. Rev. Lett. 61 (1988) 2886.
- [39] Y.R. Shen, The principles of nonlinear optics, 1st ed., Wiley, New York, 1984.
- [40] R.W. Boyd, Nonlinear optics, 1st ed., Academic Press, Boston, 1992.
- [41] Nonlinear Optics in Metals, International series of monographs on physics, K.-H. Bennemann (Ed.), Oxford University Press, Oxford, 1998.
- [42] J.E. Sipe, D.J. Moss, H.M. van Driel, Phys. Rev. B 35 (1987) 1129.
- [43] O. Keller, Phys. Rev. B 33 (1986) 990.
- [44] W. Hübner, K.H. Bennemann, K. Böhmer, Phys. Rev. B 50 (1994) 17597.
- [45] T.A. Luce, K.H. Bennemann, Phys. Rev. B 58 (1998) 15821.
- [46] W. Hübner, in K.H. Bennemann (Ed.), Nonlinear Optics in Metals, Clarendon Press, Oxford, 1998, Chap. 5.
- [47] C.M. Li, L.E. Urbach, H.-L. Dai, Phys. Rev. B 49 (1994) 2104.
- [48] G. Petrocelli, S. Martellucci, R. Francini, Appl. Phys. A 56 (1993) 263.
- [49] J. Hohlfeld, U. Conrad, E. Matthias, Appl. Phys. B 63 (1996) 541.
- [50] T. Luce, W. Hübner, K. Bennemann, Z. Physik B 102 (1997) 223.
- [51] U. Gradmann, Surf. Sci. 13 (1969) 498.
- [52] J. Shen, J. Giergil, J. Kirschner, Phys. Rev. B 52 (1995) 8454.
- [53] S. Müller, B. Schulz, G. Kostka, M. Farle, K. Baberschke, Surf. Sci. 364 (1996) 235.
- [54] Y. Chen, Z.Q. Wu, J.M. Yao, S.Y. Tong, Phys. Rev. B 39 (1989) 5617.
- [55] M.H. Mohamed, J.-S. Kim, L.L. Kesmodel, Phys. Rev. B 40 (1989) 1305.
- [56] Y. Chen, S.Y. Tong, J.-S. Kim, M.H. Mohamed, L.L. Kesmodel, Phys. Rev. B 43 (1991) 6788.
- [57] F. Huang, M.T. Kief, G.J. Mankey, R.F. Willis, Phys. Rev. B 49 (1994) 3962.
- [58] P.J. Jensen, K.H. Bennemann, Sol. State Commun. 100 (1996) 585.
- [59] W.L. O'Brien, B.P. Tonner, Phys. Rev. B 49 (1994) 15370.
- [60] V. Jähnke, U. Conrad, J. Güdde, E. Matthias, Appl. Phys. B 68 (1999) 485.
- [61] U. Conrad, J. Güdde, V. Jähnke, E. Matthias, Appl. Phys. B 68 (1999) 511.
- [62] S.Y. Tong, Y. Chen, J.M. Yao, Z.Q. Wu, Phys. Rev. B 39 (1989) 5611.
- [63] K. Baberschke, M. Farle, J. Appl. Phys. 81 (1997) 5038.
- [64] K.H. Bennemann, 1999, private communication.
- [65] American Institute of Physics Handbook, 3rd ed., D.E. Gray (Ed.), McGraw-Hill, New York, 1972.
- [66] P. Berberich, P. Hiergeist, J. Jahrstorfer, in: A. Anderson, J. Wolfe (Eds.), Phonon Scattering in Condensed Matter V, Solid-State Sciences 68, Springer, Berlin, 1986, p. 183.
- [67] R.H.M. Groeneveld, R. Sprik, A. Lagendijk, Phys. Rev. B 45 (1992) 5079.
- [68] O.B. Wright, Phys. Rev. B 49 (1994) 9985.
- [69] P.B. Allen, Phys. Rev. Lett. 59 (1987) 1460.
- [70] U. Conrad, Master's thesis, Freie Universität Berlin, 1995.
- [71] A.M. James, M.P. Lord, Macmillan's Chemical and Physical Data, The Macmillan Press Ltd, London, 1992.
- [72] C. Kittel, Einführung in die Festkörperphysik, 10th ed., R. Oldenbourg Verlag, München Wien, 1993.
- [73] Handbook of optical constants of solids, E.D. Palik (Ed.), Academic Press Handbook Series, Orlando, 1985, vol. 1.